


Design and assembly of a nested imaging X-ray telescope for the Hot Universe Baryon Surveyor mission

Jun Yu¹ , Ruohui Xian¹, Xiaoqiang Wang¹, Yifan Wang¹, Zhanshan Wang^{1*}, Wei Zhang^{1,2}, Yibo Cai², Jing Yang², Xi Lu², Wei Wang², Wei Cui^{3*}

¹*Institute of Precision Optical Engineering, Tongji University, Shanghai 200092, China*

²*Shanghai Institute of Satellite Engineering, Shanghai 201109, China*

³*Department of Astronomy, Tsinghua University, Beijing 100084, China*

*Correspondences: wangzs@tongji.edu.cn; cui@tsinghua.edu.cn

Received: January 30, 2024; Accepted: March 1, 2024; Published Online: April 18, 2024; <https://doi.org/10.61977/ati2024017>

© 2024 Editorial Office of Astronomical Techniques and Instruments, Yunnan Observatories, Chinese Academy of Sciences. This is an open access article under the CC BY 4.0 license (<http://creativecommons.org/licenses/by/4.0/>)

Citation: Yu, J., Xian, R. H., Wang, X. Q., et al. 2024. Design and assembly of a nested imaging X-ray telescope for the Hot Universe Baryon Surveyor mission. *Astronomical Techniques and Instruments*, 1(3): 157–165. <https://doi.org/10.61977/ati2024017>.

Abstract: The Hot Universe Baryon Surveyor (HUBS) mission will carry a nested X-ray telescope capable of observing an energy range from 0.5 keV to 2 keV to study hot baryon evolution. In this paper, we report the latest progress in the design and construction of nested X-ray telescopes which were designed to use a three-stage conic-approximation type assembly to simplify the manufacturing process. The mirror substrate is made using the thermal glass slumping method, with mirrors characterized by a root-mean-square roughness of 0.3 nm, with expected high reflectivity and good thermal stability. We also discuss methods of telescope construction and conduct a deformation analysis of the manufactured mirror. The in situ measurement system program is developed to guide the telescope assembly process.

Keywords: Nested X-ray telescope; Thermal glass slumping; Telescope assembly; In situ measurement

1. INTRODUCTION

High-performance X-ray telescopes have been developing rapidly since the 1970s, since the earliest X-ray telescope carried by the Uhuru satellite, the first Wolter-I structure telescope carried by the Einstein Space Observatory^[1-3], the extremely high resolution Chandra telescope^[4-6], and the XMM-Newton telescope^[7,8], as well as Suzaku^[9], NuSTAR^[10,11], eROSITA^[12], and the upcoming ATHENA telescope^[13]. While a large number of high-energy astronomical events have been observed by these telescopes, approximately 30%–50% of the baryons in the universe have not been detected, existing in the form of the Warm-Hot Intergalactic Medium (WHIM) with a temperature of 105–107 K. The most effective way to detect these hot baryons is to observe their emission or absorption lines at X-ray wavelengths. X-ray absorption lines from the WHIM have been efficiently observed by Chandra and XMM-Newton's grating spectrometers. Unfortunately, their surface brightness is lower and the coverage range is large, which makes it difficult for these existing telescopes to detect X-ray emission lines. The WHIM mainly emits OVII and OVIII lines (500–700 eV), which

are of great interest to our research.

China has proposed the HUBS mission to study “missing” baryons by detecting X-ray emission from WHIM in the universe over the next decade^[14,15]. Soft X-ray grazing incidence optics are key instrumentation in hot universe baryon observations. Owing to the weak intensity of soft X-rays emitted by hot universe baryons, a high throughput is required. To make grazing incidence optics easier to manufacture with high throughput, the angular resolution of the optical system can be relaxed. Consequently, this mission requires an X-ray telescope with a large effective area and wide field of view (FOV).

This paper introduces the design and simulation results of the X-ray telescope for HUBS and its manufacture at Institute of Precision Optical Engineering, Tongji University. For the HUBS mission, a three-stage conic-approximation type can be designed to simplify the manufacturing process. Over the past several years, we have been working to improve the capabilities of X-ray telescope imaging using manufacturing processes such as thermal glass slumping, coating fabrication, high-precision assembly, and performance evaluation. In this paper, we introduce the optical design, the basic process technology,

the mirror coating, and the telescope assembly. Section 2 describes the design and simulation results of the X-ray telescope for HUBS. Section 3 describes the hot slumping technology for manufacturing the thin mirror. Section 4 describes the bending deformation analysis of the thin mirrors, and Section 5 describes the telescope assembly and on-machine measurement technology. Finally, measurement of the latest prototype at the Shanghai Synchrotron Radiation Facility confirms that the measured resolution value of ca. 43.6'' is close to the predicted value.

2. THE PRINCIPLE AND OPTICAL DESIGN OF THE NESTED IMAGING X-RAY TELESCOPE

2.1. Nested Imaging X-ray Telescope Principle

For traditionally designed imaging X-ray telescopes, the Wolter-I (W-I) structure provides very high on-axis imaging resolution. This is because the optical structure consists of two aspherical surfaces, including paraboloid and hyperboloid mirrors, which are coaxial confocals, forming the grazing incidence reflective system. The on-axis res-

olution of the W-I structure decreases rapidly with an increasing off-axis field angle. Because the incidence angle of the grazing incidence system is very small, the light collecting area of a single mirror group has difficulty collecting enough photons to detect X-ray emission from the WHIM, so a nested X-ray telescope structure is often used to obtain a larger light collecting area. The nested W-I structure has consequently become the most commonly used X-ray telescope structure.

Considering that the manufacture of W-I structural mirrors is difficult and the curvature radii of these paraboloid and hyperboloid mirrors are very large, conical mirrors can be used to replace these aspherical surfaces. However, the errors of these conical mirrors can also reduce the axial resolution of the X-ray telescope, as shown in Fig. 1. This structure is called the conical approximate W-I structure. The ultra-thin glass can be used as a substrate material for the mirror, reducing the weight and cost of the telescope. These mirrors can be made by hot slumping technology, simplifying the processing and assembly processes. The X-ray telescope for the HUBS mission, introduced in this paper, will adopt a nested cone approximate W-I structure, and its design type is known simply as HUBS-CC.

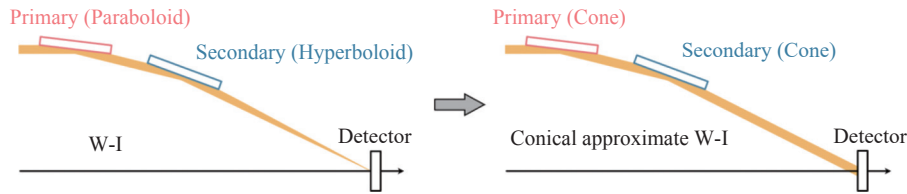


Fig. 1. Comparison of the conical approximate W-I structure and the W-I structure which it replaces.

2.2. The Optical Design Parameters of the X-ray Telescope

The independent transition-edge sensors (TESs) developed by Tsinghua University will be employed by the HUBS mission, giving a collecting area of 60×60 pixels, a pixel size of 0.7 cm^2 , and an energy resolution of $2 \text{ eV @ } 0.6 \text{ keV}$ [16]. The scientific objectives of the project are to construct this X-ray telescope with a FOV of $60'$, an imaging angular resolution of approximately $1'$ over the full FOV, an observation energy range of $0.1\text{--}1.5 \text{ keV}$, and an effective collecting area of more than $1\,000 \text{ cm}^2$ at 0.6 keV .

According to the above optical parameters, the focal length range of the system f can be calculated from the parameter values of the telescope FOV and the detector size D_{det} , using the relation

$$f \leq \frac{D_{\text{det}}}{\tan(\text{FOV})}. \quad (1)$$

The imaging angular resolution half power diameter (HPD) is proportional to the aperture of the telescope D_{tele} and inversely proportional to the square of the focal length f , as

$$\text{HPD} \propto \frac{D_{\text{tele}}}{f^2}. \quad (2)$$

The effective area on the axis field is proportional to the aperture of the telescope D_{tele} . The FOV is proportional to the aperture of the telescope D_{tele} and inversely proportional to the focal length f , as

$$\text{FOV} \propto \frac{D_{\text{tele}}}{f}. \quad (3)$$

According to the mutually restrictive relationship between the design parameters, the current telescope parameters, and the mirror manufacturing process, a design can be made to meet these requirements using the number of nested layers, mirror length, maximum aperture, and primary and secondary mirror spacing. Considering the large number of nested layers due to the required light collecting area, the telescope will be divided into an inner region and an outer region, as shown in Fig. 2. The primary and secondary mirrors of each layer of the inner region, with smaller aperture, are composed of 6 mirrors each, with the outer ring comprising 12 mirrors. Between the inner and outer regions, the 4-layer mirror region is used as a transition layer, using a wider graphite strip to

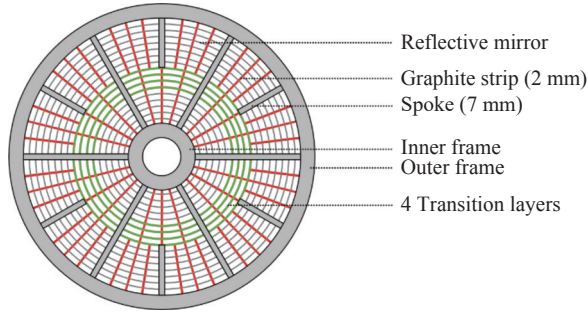


Fig. 2. The entrance pupil of the HUBS-CC telescope.

strengthen the mirror support.

The W-I and HUBS-CC structures have been designed and analyzed according to these required parameters, and the results for imaging angular resolution and

effective area are shown in Fig. 3. The resolution HPD of the W-I structure increases monotonically with the off-axis angle, while the resolution HPD of the HUBS-CC structure first decreases monotonically with the off-axis angle and then increases monotonically. For W-I structures, the defocus strategy can effectively balance the imaging resolution in the full FOV, and after defocus of -1.5 mm, the W-I structure can achieve the best resolution in the full FOV. The full field resolution of the HUBS-CC structure is better than $1''$, as shown in Fig. 3A, meeting the HUBS observation requirements. The mirror coating is platinum-based, and the effective area has been calculated as shown in Fig. 3B, and the structure and performance parameters of the HUBS-CC telescope are shown in Table 1.

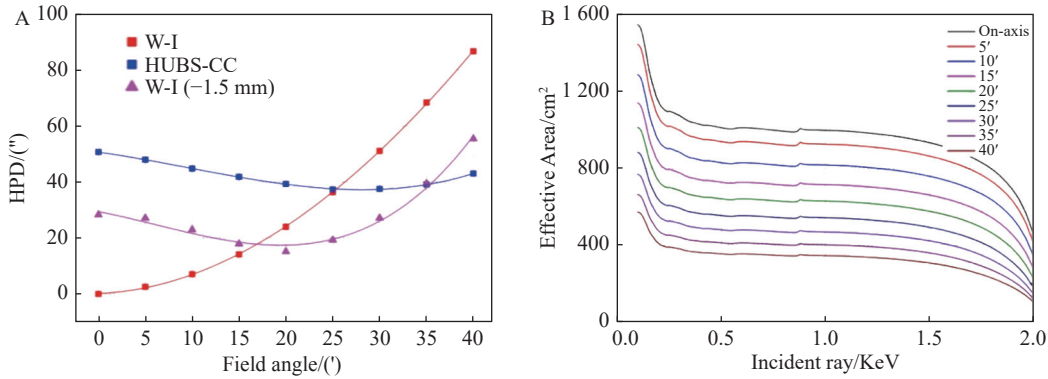


Fig. 3. The imaging angular resolution and effective area of the W-I and HUBS-CC structures.

Table 1. Parameters of the HUBS-CC telescope

Parameters	Values	Parameters	Values
Layer number, N	215	Mirror thickness	0.3 mm
Focal length, f	2 100 mm	Transition layer	107–110
Mirror length, L	50 mm	Detection area	42 mm \times 42 mm
Aperture, D	80–583 mm	Field of view	60' @ 0.6 keV
Spacing gap	4 mm	Imaging resolution	On-axis: 54'', Off-axis: 40''
Grazing incident angle, θ	0.27–1.98°	Effective area	1010 cm ² @ 0.6 keV

2.3. Stray Light Analysis

Because this X-ray telescope has a large FOV, the off-axis light may multi-reflect to form stray light, which can reach the detector and affect the imaging performance. The main kinds of stray light we consider here include primary stray light, which is only reflected by primary mirrors; secondary stray light, which is only reflected by secondary mirrors; and pass-through stray light, which enters the telescope but is not reflected by any of the telescope mirrors. Stray light is usually a problem when the incident angle is large.

The HUBS-CC telescope design also includes a series of pre-collimators, which can block stray light to reduce its impact. The length of these pre-collimators is approximately 16–39 mm, set at a distance from the primary mirror equivalent to the distance between the primary and secondary mirrors. The overall design of the telescope is a

3-segment structure, as shown in Fig. 4.

If the detector is large enough, most of the stray light it receives is primary stray light. However, because of the limited size of the detector, the imaging quality is mainly affected by secondary stray light, which is distributed on the inner side of the imaging spot, as shown in Fig. 5A. Fig. 5 also shows the comparison of stray light before

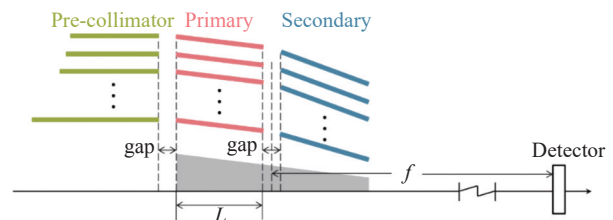


Fig. 4. Three-segment structure of the HUBS-CC telescope with pre-collimators.

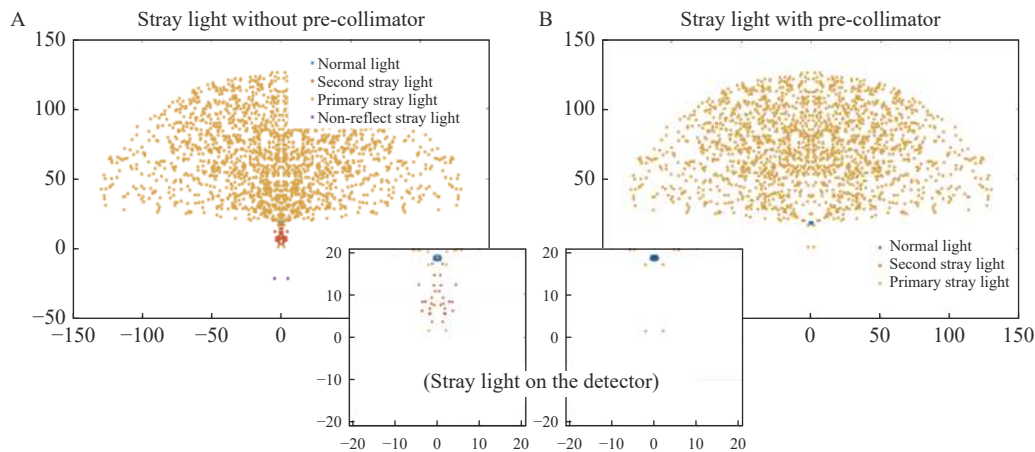


Fig. 5. Comparison diagram of stray light with and without pre-collimators (30' off-axis).

and after using the pre-collimators when the light is incident at an off-axis angle of 30'. The pre-collimators can effectively reduce the intensity of secondary stray light reaching the detector.

3. THERMAL GLASS SLUMPING TECHNOLOGY

The thermal glass slumping technology is one of the key technologies for mass processing of thin cylindrical reflective mirrors. The main principle is to place thin plate glass on a cylindrical mandrel in a hot annealing furnace, using gravity and plastic deformation during the heating process to fit the glass within the mandrel. The forming process of the thermal glass slumping is shown in Fig. 6. The mandrel is made of quartz glass, and the BN film layer is sprayed on the mandrel surface after polishing to prevent the glass from sticking. When the hot annealing furnace is heated to approximately 600 °C above the annealing temperature, the thin glass sheet will collapse under its own gravity. When the temperature in the annealing furnace returns to normal, the thin glass that has replicated the surface shape of the mandrel can be removed,

and the required working area can be accessed by hot knife cutting.

To avoid the influence of dust or debris on the surface shape of the mirror segments, the thermal glass slumping process needs to be carried out in an ultra-clean laboratory, using different types of hot forming furnaces for the large number of thin glass substrates formed at different sizes. It is also necessary to control the annealing temperature over time for the mirrors with different curvature radii. This step is to allow the mirror to optimally replicate the surface shape of the mandrel as accurately as possible. At the same time, all pre-processed thin glass must be placed in the same fixed position in the center area of the mandrel to ensure that each thin glass piece can properly replicate the mandrel surface shape, which is achieved by auxiliary positioning equipment.

In addition, the thin glass mirror is usually much larger than the size required for choosing an appropriate shape for optimal surface area. The mirror is cut to the required size after separation, using hot knife cutting technology to obtain a high-quality mirror edge without the microfractures caused by other cutting processes. The surface shape accuracy of the mirror needs to be remea-

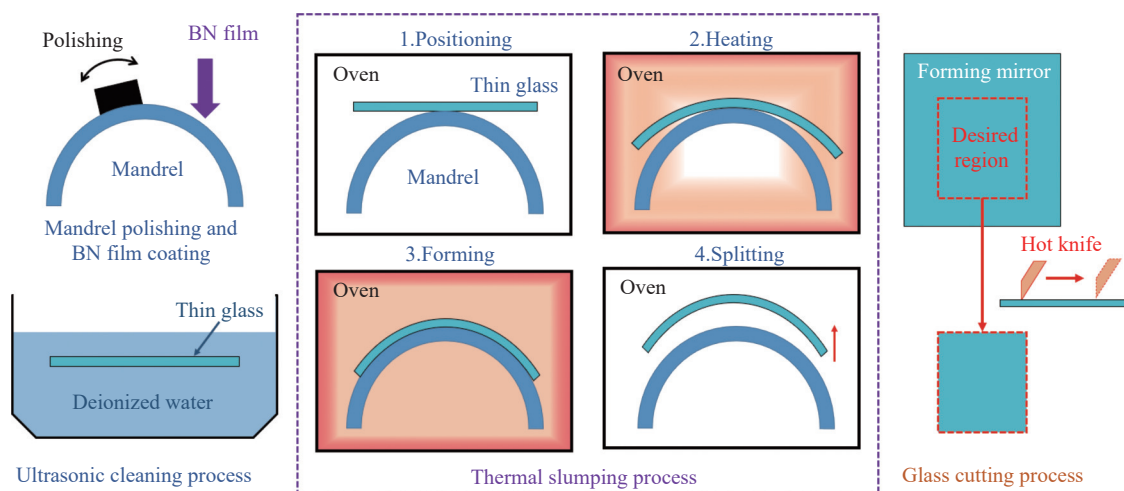


Fig. 6. The thermal glass slumping process for producing thin glass mirror segments.

sured after the cutting process. The low-frequency error of the mirror can be measured by a laser scanner and computer-generated hologram, and the high-frequency error is measured by an optical profilometer and atomic force microscopy.

4. DEFORMATION ANALYSIS OF THE THIN GLASS MIRROR

The bending of a thin glass cylindrical mirror can be mathematically modeled as being equivalent to a thin plate. The main deformation section of the thin plate during bending is in the arc region. According to the longitudinal strain analysis, when the thin plate is bending to a small curvature radius, as shown in Fig. 7A, the outer region is extended by tension, and its linear strain ε and normal stress σ are positive. While the inner region is compressed and shortened, its linear strain ε and normal stress σ are negative. The thickness of the outer layer decreases due to tensile stress, while the thickness of the inner layer increases due to compressive stress. As shown in Fig. 7B, when the curvature radius of the thin plate increases due to bending, the stress direction of the inner and outer layers changes, and the deformation changes accordingly.

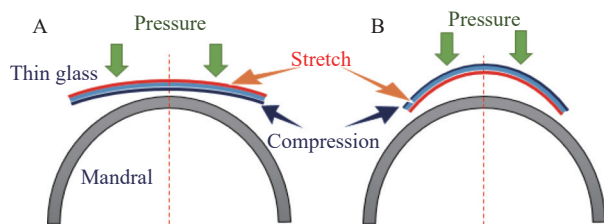


Fig. 7. Variation trend of thin mirror bending stress.

The materials selected in the thin plate bending model are isotropic. As shown in Fig. 8, the process of thin mirror bending is as follows: (1) Evenly apply epoxy resin glue to all of the graphite strips; (2) Place the thin mirror onto the mandrel; (3) Apply pressure at the points labeled 1, 2, and 3 in order, as shown in the diagram; (4) Release pressure after curing the epoxy resin adhesive. After the mirror assembly is completed, the upper surface of the graphite strip is attached to the inner layer of the thin mirror, and the surface shape of the mirror between the graphite strips is approximately conical.

The finite element method (FEM) is a highly effective engineering numerical algorithm described by the Laplace and Poisson equations that is widely used in all kinds of physical fields. If the finite element algorithm is used to simulate the thin mirror bending deformation in the early stage, the surface shape variation of the thin mirror after bending can be readily predicted, so as to provide important guidance for a more effective assembly process. To obtain accurate simulation results close to the real values, the mechanical parameters of the structural materials used in each process must be strictly controlled at the initial stage of the finite element modeling, as

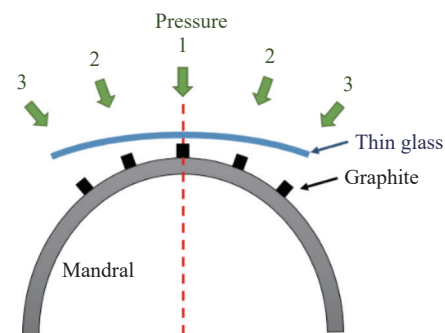


Fig. 8. Schematic diagram of thin mirror bending process.

shown in Table 2.

After affixing the graphite strips to the underside of the mirror, we perform FEM analysis, and the results are shown in Fig. 9. The maximum displacement of the mirror occurs on both sides of the section with large curvature, as shown in the deformation cloud in Fig. 9A, which is a change consistent with the trend of the previous theoretical calculation results. The larger strain area of the mirror is shown to occur between graphite strips. The closer the mirror is to both sides of the edge, the more obvious the strain is.

Table 2. Main characteristic parameters

Materials	Modulus of elasticity / (E·GPa)	Poisson's ratio/ ν	Strength limit/ (σ ·MPa)
Glass	72.9	0.208	60
Graphite	14.9	0.28	65
Rubber	0.0078	0.47	90
Aluminum	72.0	0.33	228

Fig. 10 shows the displacement cloud image of the internal reflection surface of the thin mirror along the X , Y , and Z axes. The displacement in the X direction component is the smallest, with the largest displacement mainly occurring in the Y and Z direction components. The maximum displacement in the Y direction occurs on the corners of the mirror at the side with a large curvature deviation. The displacement variation trends of the Y and Z components are similar.

Fig. 10D shows the surface error between the simulated inner surface after mirror bending and the ideal surface. The displacement cloud image shows that the surface deviation value is the smallest at the five adhesive sections. The surface error in the edge regions belongs to the free bending section, and this non-glass effective working area is not considered. In the unbonded regions, due to the elastic deformation of the thin mirror surface under adhesive force, the deviation value near the symmetric plane, the axial warping range near the symmetric plane (40–100 mm), and the axial warping range near the symmetric plane (20–100 mm) are all relatively small. The general trend is that the surface deviation of the middle section is smaller, while the surface deviation on either side is larger. The greater the curvature, the larger the deviation.

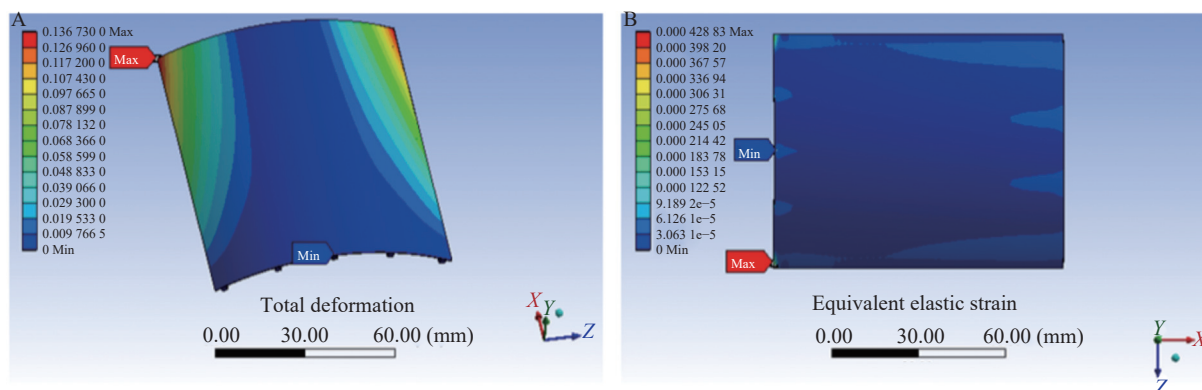


Fig. 9. Displacement and strain cloud of thin mirror after bending process.

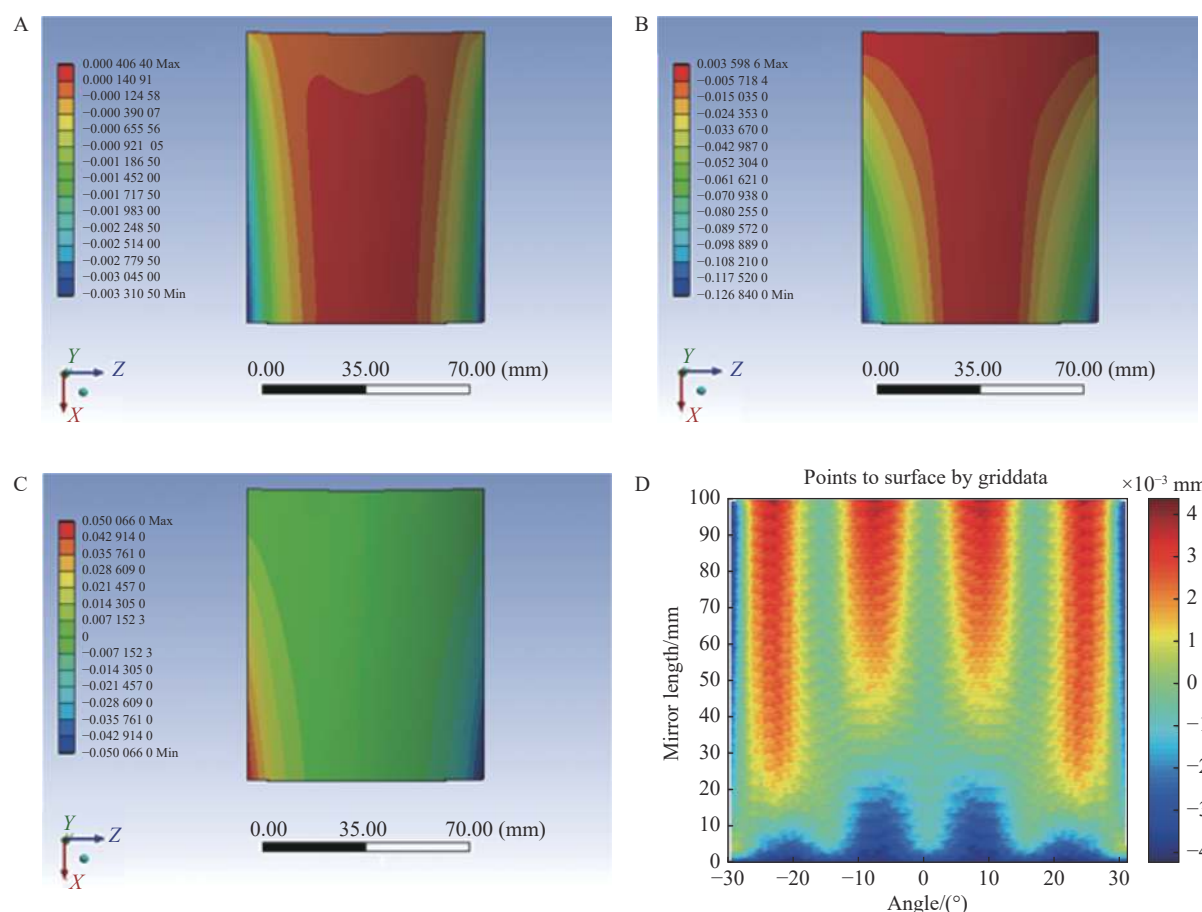


Fig. 10. Displacement of the inner surface of the thin mirror after bending.

tion. According to the FEM analysis, the maximum surface shape deviation between the thin and ideal mirrors is approximately $4\text{ }\mu\text{m}$.

5. ASSEMBLY AND ON-MACHINE MEASUREMENT TECHNOLOGY

The D263 glass produced by SCHOTT has been used as the mirror substrate for the HUBS-CC telescope. As described in Section 3, this plate glass is molded in the ther-

mal glass slumping process, and the cylindrical shape of the mandrel is replicated. After the multilayer coating is applied, the cylindrical mirror is affixed to the conical surface using a pressure-gluing process.

During the thin mirror manufacture processing and assembly process, the original surface shape of the mirror needs to be measured several times, including after hot bending, after hot knife cutting, and both before and after coating. This process continues into the later stages of assembly, when the surface shape is measured using an on-machine method. These measurements play a very

important role in evaluating the surface shape of thin mirrors at various stages of the manufacturing process and in optimizing the iterative manufacturing process.

5.1. Precision Assembly of Nested X-ray Telescope

The overall development process of the X-ray telescope, using thermal glass slumping, is summarized in Fig. 11. After the design, manufacture, and multilayer coating described above, the next step for the telescope mirrors is precision assembly. This involves the accurate and stable installation of all mirrors in carefully optimized positions.

First, the aluminum mandrel is machined on an ultra-precision single-point diamond lathe. To reduce gravity deformation of the mandrel and improve assembly accuracy, we added a tailstock to the Nanotech 450UPL ultra-

precision diamond turning lathe. Second, the graphite strips are bonded to the surface of the mandrel at specified positions, and the surface shape of the outer layer is finished with a high-speed grinding wheel. The mirror is glued to the processed graphite strips using uniform pressure to achieve accurate positioning and molding. The assembly process is repeated several times in sequence to complete the assembly of the entire telescope. It should be noted that the epoxy resin adhesive is a viscous fluid during its curing process, and its uniformity should be ensured to achieve the highest possible assembly accuracy. To optimize the bonding process, we designed a uniform load device that uses air pressure to provide a uniform pressure to the curvature of the mirror. After the best process parameters have been selected, the final thickness accuracy of the cured epoxy resin layer is ca. 1 μm .

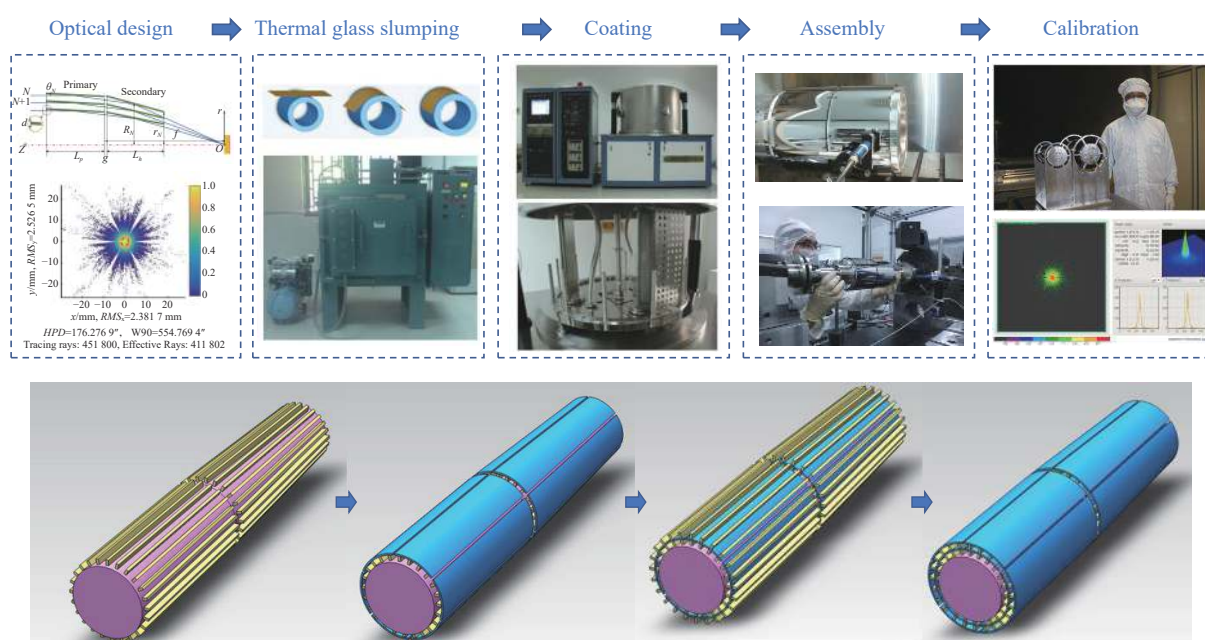


Fig. 11. Nested X-ray telescope assembly process.

Over the past decade, the manufacture of nested X-ray telescopes has improved based on the thermal glass slumping method, X-ray coating technology, high-precision assembly, and performance evaluation methods. At present, we are able to mass-produce cylindrical mirror substrates with an angular resolution of 10". To increase the effective area of the mirror, C, Ni, and Pt coatings can be used to achieve high reflectivity in the range of 0.5–2 keV. In the optical assembly process, we have developed an on-machine measurement system and a 3D ray tracing program to guide the assembly process in real time^[17].

5.2. On-machine Measurement after Thin Mirror Assembly

The reflective surface of a nested X-ray telescope is the lower surface of the mirror. Fig. 12A illustrates the indirect on-machine measurement process for the lower surface. The indirect measurement process first obtains the surface shape data of the upper surface using a white light con-

focal detector in range working mode, then obtains the mirror thickness deviation data in interferometric mode, and subtracts the mirror thickness deviation data from the mirror upper surface data to obtain the true surface shape of the lower surface. This method is an effective way to measure the lower surface of the mirror when the mirror thickness is not consistent. Fig. 12B and Fig. 12C show the results of an on-machine measurement, yielding the surface shape of a mirror mounted on a telescope. The results show that the bending trend is consistent with that of the FEM simulation. The surface deviation peak-to-valley (PV) and root-mean-square (RMS) values are close to 4 μm and 1 μm , respectively.

6. MEASUREMENT RESULT

The HUBS prototype is tested at the Shanghai Synchrotron Radiation Facility at an energy of 8 keV. In this energy range, scattering and absorption are small, so the

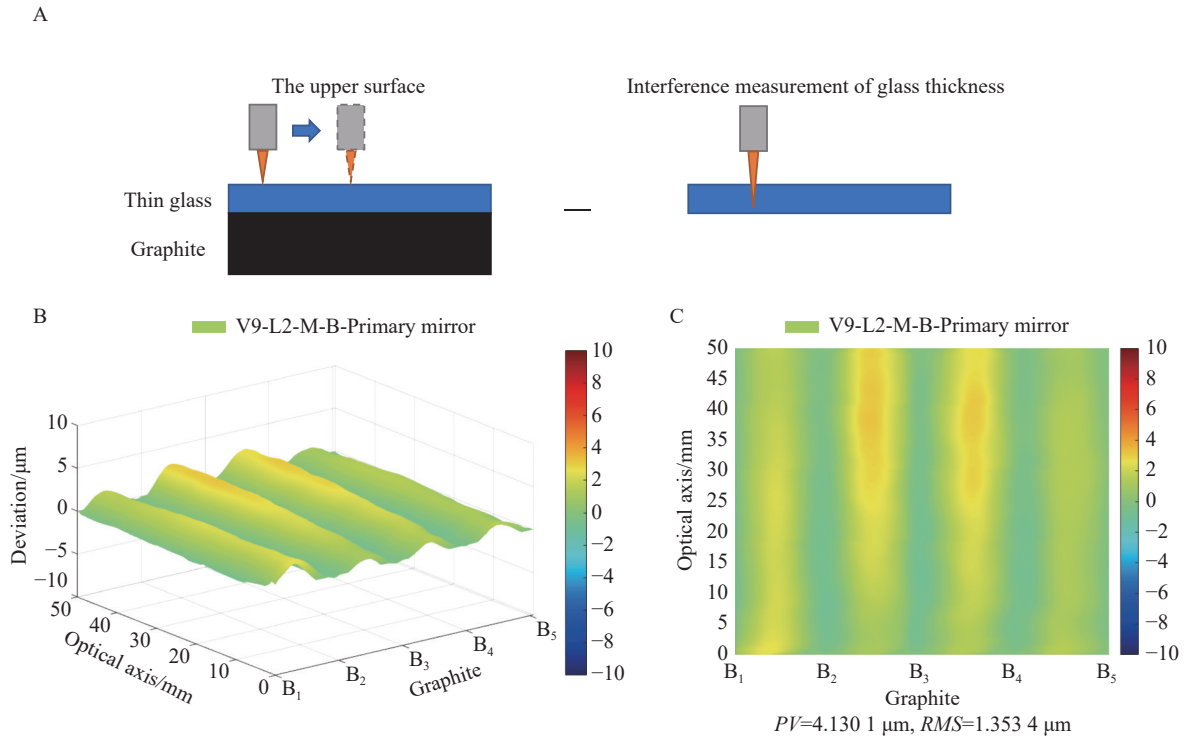


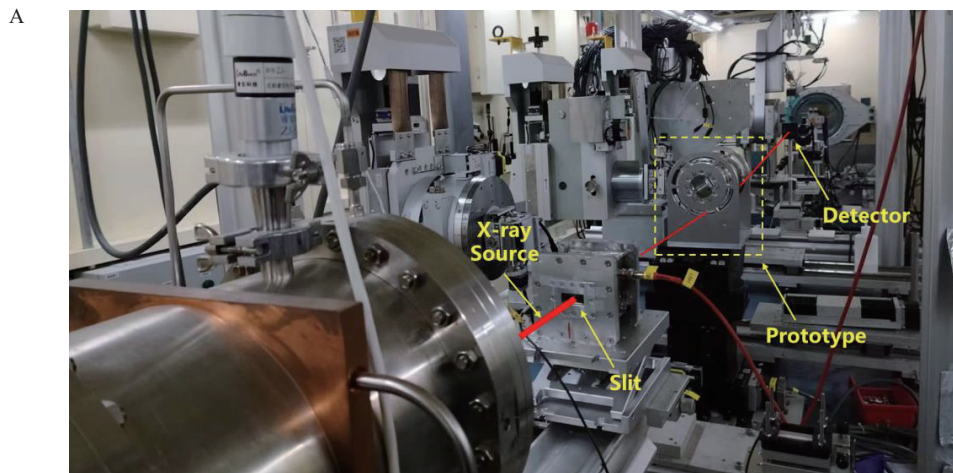
Fig. 12. The surface shape obtained by the on-machine measurement.

test can be carried out without vacuum conditions, effectively reducing the calibration difficulty. To give uniform irradiance, the X-ray source is passed through a slit. The telescope prototype is then mounted onto multi-axis moving stages and aligned to the emitted X-rays, as shown in Fig. 13A. The detector positions are moved along the optical axis to find the best focal plane during the scan. As shown in Fig. 13B and Fig. 13C, the simulated resolution is approximately 40", and the measured resolution result is ca. 43.6". This value difference is less than 10%, which is mostly accounted for by scattering, alignment, and measurement errors.

7. CONCLUSION

The HUBS satellite will use a nested conical W-I struc-

ture for X-ray imaging, with the X-ray telescope designed as a three-stage structure to effectively suppress the influence of off-axis stray light and improve detection sensitivity. The nested X-ray optical system consists of a large number of reflecting mirrors, which need to be precisely stacked together to give an optimal light collection area. This results in a challenging assembly process. We have carried out extensive work on thin glass mirror manufacturing technology, X-ray coating technology, precision assembly, and measurement methods. Our precision assembly technology, based on the thermal glass slumping method, allows high-precision integrated assembly of the telescope. FEM simulations of thin mirror bending deformation are consistent with the experimental results, and the maximum deviation PV value between the manufactured mirror and the ideal surface shape can be controlled at approximately 4 μm. As the development of the HUBS mis-



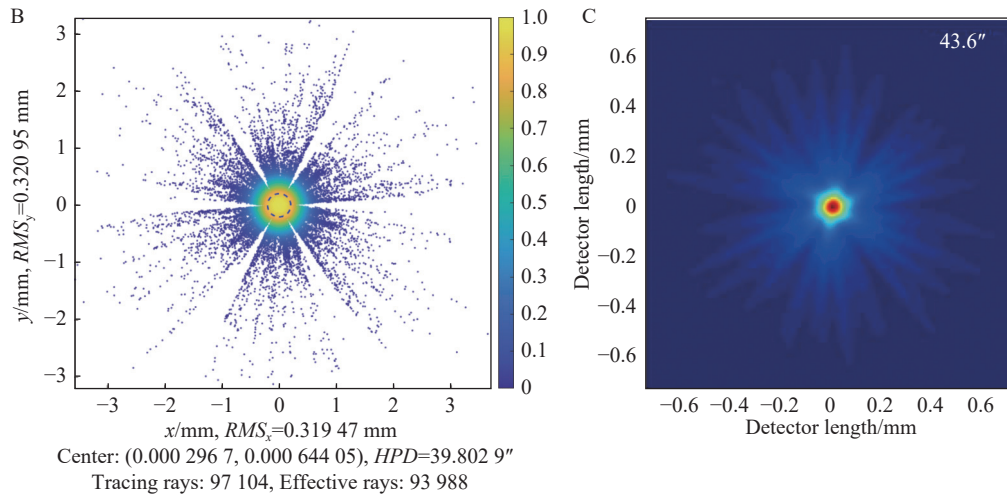


Fig. 13. The optical prototype at the Shanghai Synchrotron Radiation Facility.

sion progresses, we will further improve the relevant core technologies, which will facilitate the engineering progress of the project.

ACKNOWLEDGEMENTS

This work is supported by National Key R&D Program of China (2022YFF0709101); China National Space Administration (D050104); National Natural Science Foundation of China (62105244 and U2030111).

AUTHOR CONTRIBUTIONS

Jun Yu and Ruohui Xian conceived the idea, provided investigation support, wrote original draft and edited the manuscript. Zhanshan Wang and Wei Cui reviewed the manuscript, and played the project administration and supervision role. Wei Wang, Xi Lu and Wei Zhang reviewed the manuscript and played the supervision role. Yibo Cai, Jing Yang, Xiaoqiang Wang and Yifan Wang provided investigation support. All authors read and approved the final manuscript.

DECLARATION OF INTERESTS

Xi Lu is an editorial board member for Astronomical Techniques and Instruments and was not involved in the editorial review or the decision to publish this article. The authors declare no competing interests.

REFERENCES

- [1] Tananbaum, H., Gursky, H., Kellogg, E. M., et al. 1972. Discovery of a Periodic Pulsating Binary X-Ray Source in Hercules from UHURU. *The Astrophysical Journal*, **174**(6): L143–L149.
- [2] Giacconi, R., Branduardi, G., Briel, U., et al. 1979. The Einstein (HEAO 2) X-ray observatory. *The Astrophysical Journal*, **230**(6): 540–550.
- [3] Van Speybroeck, L. P. 1979. Einstein Observatory (HEAO-B) mirror design and performance. In *Proceedings of SPIE*. 184: 2–11.
- [4] O'Dell, S. L., Bautz, M. W., Blackwell, W. C., et al. 2000. Radiation environment of the Chandra X-ray Observatory. In *Proceedings of SPIE*. 4140: 99–110.
- [5] Weisskopf, M. C., Tananbaum, H. D., Van Speybroeck, L. P., et al. 2000. Chandra X-ray Observatory (CXO): overview. In *Proceedings of SPIE*. 4012: 2–16.
- [6] Weisskopf, M. C., Brinkman, B., Canizares, C., et al. 2002. An overview of the performance and scientific results from the Chandra X-Ray Observatory. *Publications of the Astronomical Society of the Pacific*, **114**(1): 1–24.
- [7] Aschenbach, B., Briel, U. G., Haberl, F., et al. 2000. Imaging performance of the XMM-Newton X-ray telescopes. In *Proceedings of SPIE*. 4012: 731–739.
- [8] Aschenbach, B. 2002. In-orbit performance of the XMM-Newton X-ray telescopes: images and spectra. In *Proceedings of SPIE*. 4496: 8–22.
- [9] Mitsuda, K., Bautz, M., Inoue, H., et al. 2007. The X-ray observatory Suzaku. *Publications of the Astronomical Society of Japan*, **59**(1): S1–S7.
- [10] Koglin, J. E., Christensen, F. E., Craig, W. W., et al. 2005. NuSTAR hard X-ray optics. In *Proceedings of SPIE*. 5900: 266–275.
- [11] An, H. J., Christensen, F. E., Doll, M., et al. 2009. Evaluation of epoxy for use on NuSTAR optics. In *Proceedings of SPIE*. 7437: 74371J.
- [12] Menz, B., Bräuninger, H., Burkert, W., et al. 2013. Alignment of eROSITA like mirrors at the PANTER X-ray test facility. In *Proceedings of SPIE*. 8861: 88611I.
- [13] Barcons, X., Nandra, K., Barret, D., et al. 2015. Athena: the X-ray observatory to study the hot and energetic Universe. *Journal of Physics: Conference Series*, **610**(1): 012008.
- [14] Cui, W., Chen, L. B., Gao, B., et al. 2020. HUBS: Hot Universe Baryon Surveyor. *Journal of Low Temperature Physics*, **199**(1/2): 502–509.
- [15] Zhang, Y. N., Li, C. Z., Xu, D. D., et al. 2022. Mock HUBS observations of hot gas with IllustrisTNG. *Experimental Astronomy*, **53**(4): 1053–1074.
- [16] Wang, Y. R., Wang, S. F., Li, F. J., et al. 2020. Development of TES-based X-ray microcalorimeters for HUBS. *Proceedings of Society of Photo-Optical Instrumentation Engineers (SPIE)*, **11444**: 114449C.
- [17] Yu, J., Shen, Z. X., Sheng, P. F., et al. 2018. Ray tracing method for the evaluation of grazing incidence x-ray telescopes described by spatially sampled surfaces. *Applied Optics*, **57**(7): B74–B82.